Smeared crack approach: back to the original track

M. Cervera and M. Chiumenti

International Center for Numerical Methods in Engineering (CIMNE)

Technical University of Catalonia (UPC)

Edificio C1, Campus Norte, Jordi Girona 1-3, 08034 Barcelona, Spain.

Abstract

This paper briefly reviews the formulations used over the last 40 years for the solution of problems involving tensile cracking, both with the discrete and smeared crack approaches. The paper focuses in the smeared approach, identifying as its main drawbacks the observed mesh-size and mesh-bias spurious dependence when the method is applied "straightly". A simple isotropic local damage constitutive model is considered, and the (exponential) softening modulus is regularized according to the material fracture energy and the element size. The continuum and discrete mechanical problems corresponding to both the weak discontinuity (smeared cracks) and strong discontinuity (discrete cracks) approaches are analyzed and the question of propagation of the strain localization band (crack) is identified as the main difficulty to be overcome in the numerical procedure. A tracking technique is used to ensure stability of the solution, attaining the necessary convergence properties of the corresponding discrete finite element formulation. Numerical examples show that the formulation derived is stable and remarkably robust. As a consequence, the results obtained do not suffer from spurious mesh-size or mesh-bias dependence, comparing very favorably with those obtained with other fracture and continuum mechanics approaches.

1 Introduction

Cracking is an essential feature of the behaviour of concrete structures and, therefore, tensile cracking must be taken into account in predicting their ultimate load capacity as well as service behavior.

The tensile fracture of concrete is regarded as (quasi)brittle. Concrete has no yield behavior as exhibited by metals. Its tensile stress-strain diagram is nearly linear up to the peak stress, whereupon it immediately starts to descent. In spite of this, concrete shows considerable toughness. This toughness is related to the existence of a descending branch in the nominal stress-strain curve. This is known as strain softening.

With the advent of digital computers and computational mechanics, two different concepts of the phenomenon of tensile cracking have evolved: the *discrete* and the *smeared crack approaches*. Although nowadays many structural engineers and computational solid FE codes are decanted in favor of the smeared crack approach, the observed mesh-size and mesh-bias dependence make the academic world very suspicious about the solutions obtained within this format. A lot of effort has been spent in the last 40 years to investigate and remedy the observed drawbacks of this approach.

In recent papers ([1] and [2]) it is shown that mesh objective solutions, convergent upon refinement and exhibiting highly localized shear bands (or slip lines), can be obtained using local J_2-plasticity and damage models. This is achieved by (i) using the suitable mixed format of the balance equations and (ii) using an stabilization technique especially designed to stabilize the selected interpolation fields for the primary variables (displacements and pressure). Hence, it may be concluded that with the appropriate continuum framework and with local constitutive models, the problem can be solved if the shortcomings of the spatial discretization used are satisfactorily surmounted.

As a consequence, the objectives of this paper are threefold: (i) to *investigate the numerical difficulty* that causes the mesh bias encountered in tensile localization problems when using the classical smeared crack approach, (ii) to *propose an auxiliary numerical procedure* to overcome the identified numerical difficulty, and (iii) to *assess the performance* of the proposed procedure by means of solving selected numerical examples which exhibit tensile cracking.

The outline of the paper is as follows. In the next section we briefly review the main historical developments occurred both in the discrete and smeared crack approaches in the last decades. Then, a simple isotropic scalar

Rankine damage model, suitable for degradation under tensile straining, is presented. The necessary regularization of the softening modulus according to the size of the elements inside the localization band is discussed. Later, the corresponding standard irreducible boundary value problems for the so-called *weak and strong discontinuity approaches* are formulated. Also, the well-known difficulties of solving localization problems using the standard, weak discontinuity, local formulation are explained. Tracking of the crack through the fixed FE mesh is presented as a remedy to overcome this last difficulty. Finally, selected numerical examples are presented to assess the present formulation and to show the attained benefits as compared to the "straight" use of the standard local formulation.

2 Discrete and smeared crack approaches

2.1 Discrete crack approach

In the earliest applications of the FEM to concrete structures, back in the 1960's ([3], [4], [5]), cracks were modelled discretely (DC), by separation of nodal points initially occupying the same spatial position. An obvious restriction of such models is that cracks can only be formed along the element boundaries (Fig. 1a). Thus, the response is strongly mesh-dependent. Furthermore, when a crack propagates, the topology of the mesh is changed, and the updating procedures are time consuming. The DC approach was later refined so that new elements could be introduced whose boundaries were along the spreading crack (Fig. 1b). This obviously reduces the mesh dependency of the approach, but then remeshing techniques are required and the computing time increases.

Although the primitive studies had been based in a simple maximum tensile stress criterion to decide on the moment of crack propagation, it was recognized very early that the stress and strain fields that develop at the tip of the crack are singular and stress criteria were not reliable. Crack propagation was then based on energy criteria. Also, it was noted that standard FE were not appropriate to capture these singular stress and strain fields [6]; consequently, special FE were developed (see reference [7]).

Alternatively, in the last decade, an effort has been made to tackle the discretization problem directly. Recently, Belytschko and coworkers ([8], [9], [10]) have introduced the so-called *extended finite element method* (X-FEM),

which effectively overcomes most of the cited disadvantages of the DC approach. The X-FEM allows for crack propagation without remeshing, at the expense of tracking the advance of the crack through the FE mesh and progressively enriching the nodal degrees of freedom with new ones that represent both the *displacement jumps across the crack* and the developed *singular field at the tip* of the advancing crack (Fig. 1c, where the "enriched" nodes are marked).

Another of these efforts to model discrete cracks without the need of remeshing is the so-called *strong discontinuity approach* ([11], [12], [13], [14], [15], [16]). The strong discontinuity concept does not really depart from the usual continuum mechanics framework (its theoretical formulation is very similar to that of contact problems) but it leads to new formulations for finite elements with *embedded discontinuities*, depending on the kinematical and statical assumptions adopted. Interestingly enough, their application invariably needs the use of *tracking* algorithms ([14], [16], [17], [18]), in order to establish which elements lie in the crack path and need to be enriched
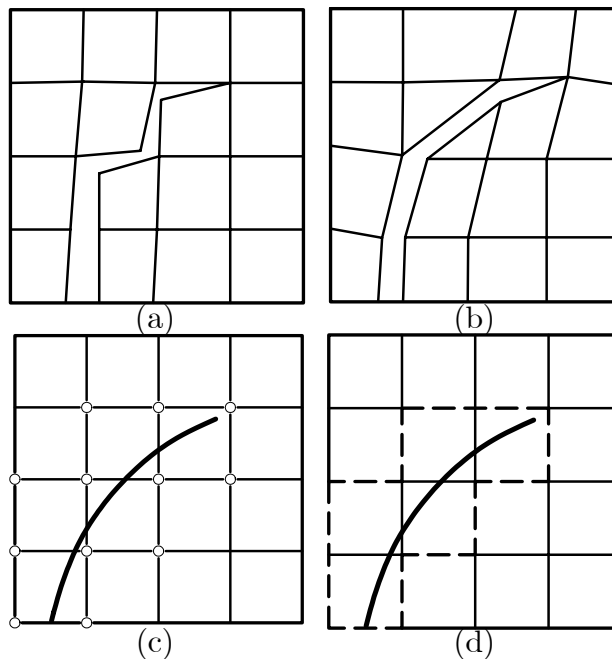

Figure 1: Discrete approaches to crack propagation: (a) without remeshing, (b) with remeshing, (c) with nodal enrichment and (d) with elemental enrichment

(Fig. 1d, where the elements with "embedded" discontinuities are marked). This, as the explicit control on the energy dissipated in the formation of the crack, represents another link with the well established tradition of fracture mechanics.

2.2 Smeared crack approach

The smeared crack (SC) approach comes directly from computational continuum mechanics. This means that, at least initially, the criteria for crack propagation and, eventually, the prediction of the direction of propagation came directly from this theory, which is, mostly, based on failure criteria expressed in terms of stresses or strains. SC models do not account for discontinuities in the topology of the FE mesh, so remeshing is unnecessary (Fig. 2a). On the contrary, the cracked material is assumed to remain a continuum and the mechanical properties (stiffness and strength) are modified to account for the effect of cracking, according to the evolving states of strain and/or stress. This leads to the concept of generalized constitutive models, strongly nonlinear and with strain softening.

This approach was first used by Rashid in his 1968 historical paper [19] to study prestressed concrete pressure vessels. It must be said that the simplicity of this concept caught the attention of the engineering community immediately and, during many years, the smeared crack concept practically monopolized the field of crack propagation. The approach can be implemented in any nonlinear FE code by simply writing a routine for a new
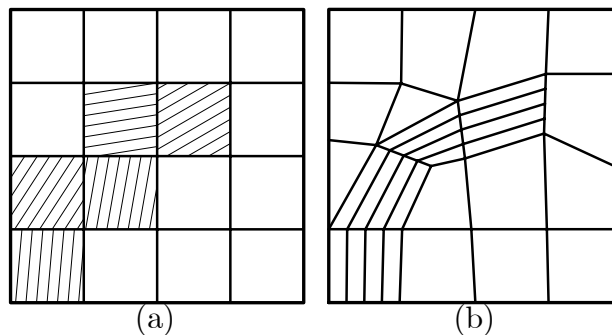

Figure 2: Smeared approaches to crack propagation: (a) without remeshing and (b) with remeshing

material constitutive model. Even today, more than 35 years later, most of the commercial FE codes use this approach, with little refinement over the original Rashid's ideas.

Unfortunately, it was realized in the 1970's that if a smeared crack is only one element across, the total energy dissipated in the cracking process is proportional to the size (the volume) of the element. Upon mesh refinement, for infinitesimally small elements, the dissipated energy vanishes. This is unacceptable from the physical point of view. The problem was satisfactorily solved in 1983, when Bazant and Oh [21] proposed the *crack band model*, which is essentially identical to the previous Hillerborg's [20] *cohesive crack model*, but developed in the context of continuum mechanics and, therefore, easily implemented in standard FE codes. These models showed that the always controversial concept of *strain softening* should not be considered as a characteristic of the material, but it is related to the *fracture energy* of the material and the *size of the FE* crossed by the smeared crack. Today, most of the commercial FE codes implement models with strain softening according to this idea of relating the dissipated energy to the fracture energy of the material.

In the 1980's, the constitutive models used were mostly orthotropic and max. principal stress driven. A lot of effort was devoted to the apparent "stress locking" effect that was observed when the directions of principal strain rotated along the analysis. Reference [22] presents a review of damage-based approaches for the fracture of quasi-brittle materials, linking them to the now old-fashioned, although still very popular, fixed and rotating smeared crack models of those years.

Since the 1990's, isotropic damage or plasticity models are usually preferred to model crack propagation. This choice implies that the macroscopic anisotropy of the structural behaviour has to be captured by means of the finite element approximation to within the resolution of the adopted mesh ([23], [24], [25]).

But once the problem of mesh-size dependence was quite satisfactorily overcome, a more difficult one was recognized. FE solutions based on SC suffer from mesh-bias dependence in such a strong manner that it can not be ignored. However, if the spatial discretization is designed in such way that an "appropriate" path for the advancing crack is available, the solutions obtained are satisfactory (see Fig. 2b). The well-known fact that "well-aligned" meshes produce good results strongly suggests that the difficulty lies in the spatial discretization procedure.

However, this evidence has not been generally recognized. Up to now, the disagreeable effects of mesh dependence have been attributed to the fact that, when strain-softening occurs and the slope of the local stress-strain curve becomes negative, the governing equations of the continuum problem lose their "natural" elliptic character. To remedy this, many so-called *non-local* constitutive models have been proposed in the last decade in different versions (*micropolar* models ([26]), *gradient-enhanced* models ([26], [27], [28], [29], [30])). All these strategies introduce a "localization limiter" (a length parameter) into the problem that effectively precludes the occurrence of sharp displacement gradients (strains).

3 Isotropic Rankine damage model

3.1 Constitutive model

The constitutive equation for the isotropic damage model is defined as:

$$\boldsymbol{\sigma} = (1 - d)\,\overline{\boldsymbol{\sigma}} \;=\; (1 - d)\,\mathbf{C} : \boldsymbol{\varepsilon} \tag{1}$$

where the effective stresses $\overline{\boldsymbol{\sigma}}$, $\overline{\boldsymbol{\sigma}} = \mathbf{C} : \boldsymbol{\varepsilon}$, can be computed in terms of the total strain tensor $\boldsymbol{\varepsilon}$, $\boldsymbol{\varepsilon} = \nabla^s \mathbf{u}$, where $\mathbf{u}$ are the displacements, (:) denotes the double contraction and d, the damage index, is an internal-like scalar variable whose definition and evolution is given below.

In the present work, the *equivalent stress* will assume the following form:

$$\tau = \langle\, \bar{\sigma}_1 \,\rangle \tag{2}$$

where $\bar{\sigma}_1$ is the largest principal effective stress and $\langle \cdot \rangle$ are the Macaulay brackets ($\langle x \rangle = x$, if $x \geq 0$, $\langle x \rangle = 0$, if $x < 0$).

With this definition for the equivalent effective stress, the damage criterion, Φ, is introduced as:

$$\Phi\left(\tau, r\right) = \tau - r \leq 0 \tag{3}$$

where r is an internal stress-like variable that is interpreted as the current damage threshold, in the sense that its value controls the size of the (monotonically) expanding damage surface. The initial value of the damage threshold is $r_o = \sigma_o$, where σ_o is the initial uniaxial damage stress.

The expansion of the damage bounding surface for loading, unloading and reloading conditions is controlled by the Kuhn-Tucker relations and the damage consistency condition, which are

$$\dot{r} \;\geq\; 0 \qquad \Phi\left(\tau,r\right) \leq 0 \qquad \dot{r}\,\Phi\left(\tau,r\right) = 0 \qquad \text{(4a)}$$

$$\text{if } \Phi\left(\tau,r\right) = 0 \;\text{ then }\; \dot{r}\,\dot{\Phi}\left(\tau,r\right) = 0 \qquad \text{(4b)}$$

leading, in view of Eq. (3), to the loading condition

$$\dot{r} = \dot{\tau} \qquad (5)$$

This, in turn, leads to the explicit definition of the current values of the internal variable r in the form

$$r \;=\; \max\left\{\, r_o,\, \max\left(\tau\right)\right\} \qquad (6)$$

Finally, the damage index $d = d(r)$ is explicitly defined in terms of the corresponding current value of the damage threshold, so that it is a monotonically increasing function such that $0 \leq d \leq 1$. In this work, we will use the following exponential function:

$$d(r) = 1 - \frac{r_o}{r}\,\exp\left\{-2H_S\left(\frac{r - r_o}{r_o}\right)\right\} \qquad r_o \leq r \qquad (7)$$

where $H_S \geq 0$ is the softening parameter.

3.2   Strain-softening and fracture width regularization

In FE analysis, the straight use of strain softening constitutive models entails the loss of objectivity of the results, in the sense that the strains tend to localize in a band that is only one element across, independently of the element size h_e. Upon mesh refinement, as h_e tends to zero, strains tend to concentrate on a band of zero thickness (a geometrical line), and no energy is dissipated in the failure process. Clearly, this is physically unacceptable.

In order to remedy this well-accounted for fact, Bazant and Oh [21] proposed the use of the so-called *fracture energy regularization technique*, nowadays used in many FE applications. This technique is based on the assumption that dissipation takes place in a band only one element thickness, irrespective of the element size. The basic concept consists on modifying the softening law in such a way that the energy dissipated over a completely

degraded finite element be equal to a given value, which depends on the fracture energy of the material and on the element size.

In each element, the computational width of the fracture zone is called the *element characteristic length* l_{ch} [31]. The specific dissipated energy $\mathcal{D}$ is then adjusted for each element so that the equation

$$\mathcal{D}\, l_{\mathrm{ch}} = \mathcal{G}_f \tag{8}$$

holds, where $\mathcal{G}_f$ is the mode I fracture energy of the material, regarded to be a material property. This makes the softening modulus H_S dependent on the element size.

For the isotropic damage model with exponential softening it can be proved that the specific dissipated energy is

$$\mathcal{D} = \left(1 + \frac{1}{H_S}\right) \frac{\sigma_o^2}{2E} \tag{9}$$

and, therefore

$$H_S = \frac{\overline{H}_S\, l_{\mathrm{ch}}}{1 - \overline{H}_S\, l_{\mathrm{ch}}} \qquad \geq 0 \tag{10}$$

where $\overline{H}_S = \sigma_o^2 / \left(2E\mathcal{G}_f\right)$ depends only on the material properties, as $\mathcal{G}_f$ is the mode I fracture energy per unit area, σ_o is the uniaxial strength and E is the Young's modulus. For linear simplicial elements, the characteristic length can be taken as the representative size of the element, $l_{\mathrm{ch}} = h_e$. Assuming that the elements are equilateral, the size of the element can be computed as $h_e^2 = \left(4/\sqrt{3}\right) A_e$ for triangular elements, A_e being the area of the element.

It is clear from Eq. (10) that this calibration procedure implies a limitation on the maximum size of the finite elements used in the mesh, $h_e \leq 1/\overline{H}_S$, which depends only on the material properties. For a given set of material properties, the larger the elements, the steeper would be the softening branch of the response, and, locally, the fracture process would be more brittle. For $h_e > 1/\overline{H}_S$ the dissipated energy $\mathcal{D} = \mathcal{G}_f/h_e$ is smaller than the elastic energy stored by the element, and fracture cannot occur quasi-statically.

It is remarkable how this simple technique solves the problem of mesh-size dependence satisfactorily. To show this, consider the 1D problem of a straight bar under tensile straining, with a small defect located at a given position inside the bar. Obviously, the only reasonable solution is a crack initiating and progressively opening at the location of the defect. If the problem is solved with small enough time increments so to ensure that only the finite

9

element containing the defect opens at the proper time step, and the element size is adequately taken into account to regularize the local softening, the global response of the bar, in terms of load vs. end displacement is unique and perfectly objective upon mesh refinement.

4   Boundary value problem

The possibilities to model tensile cracks with finite elements within the continuum mechanics framework are several, and both the weak and the strong discontinuity approaches have been followed. In the first one, the objective is to capture the crack as a discontinuity in the strain field, using standard continuous elements; the smeared crack approach is included in this category. In the second one, the displacement field of the element is enhanced with discontinuous functions so that the actual jump in the displacement field can be captured. In fact, both approaches are compatible. On one hand, a weak discontinuity can be interpreted as the regularization of a strong one over a given width, for instance with the discontinuity "smeared" across the maximum possible resolution of the mesh, that is, one element; on the other hand, a strong discontinuity is the limit case of a weak one with vanishing
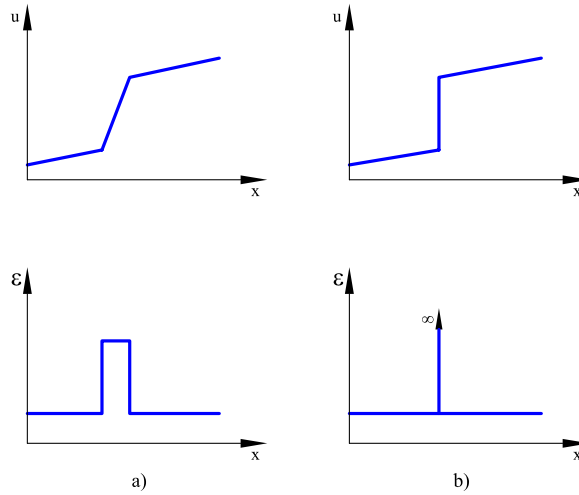

Figure 3: Strain localization: (a) weak (strain) discontinuity; (b) strong (displacement) discontinuity

width. Figure 3a sketches both approaches to strain localization.

4.1 Weak and strong discontinuity approaches

4.1.1 Weak (strain) discontinuity approach

The strong form of the continuum mechanical problem can be stated as: find the displacement field $\mathbf{u}$, for given prescribed body forces $\mathbf{f}$, such that:

$$\nabla \cdot \boldsymbol{\sigma} + \mathbf{f} = \mathbf{0} \qquad \text{in } \Omega \tag{11}$$

where Ω is the open and bounded domain of $\mathbb{R}^{n_{\dim}}$ occupied by the solid in a space of $n_{\dim}$ dimensions. Eq. (11) is subjected to appropriate Diritchlet and Neumann boundary conditions. In the following, we will assume these in the form of prescribed displacements $\mathbf{u} = \overline{\mathbf{u}}$ on $\partial\Omega_u$, and prescribed tractions $\overline{\mathbf{t}}$ on $\partial\Omega_t$, respectively.

Multiplying by the test functions and integrating by parts, the associated weak form of the problem can be stated in the standard form as:

$$(\nabla^s \mathbf{v}, \boldsymbol{\sigma}) - (\mathbf{v}, \mathbf{f}) - (\mathbf{v}, \overline{\mathbf{t}})_{\partial\Omega_t} = 0 \qquad \forall \mathbf{v} \qquad \text{in } \Omega \tag{12}$$

where $\mathbf{v} \in \mathcal{V}$ are the variations of the displacement field, $\mathcal{V}$ is the space of functions in $\mathbf{H}^1(\Omega)$, that is, functions square integrable in Ω with square integrable derivatives, that vanish on $\partial\Omega_u$; $(\cdot, \cdot)$ denotes the inner product in $L^2(\Omega)$.

The corresponding discrete problem is

$$(\nabla^s \mathbf{v}_h, \boldsymbol{\sigma}_h) - (\mathbf{v}_h, \mathbf{f}) - (\mathbf{v}_h, \overline{\mathbf{t}})_{\partial\Omega_t} = 0 \qquad \forall \mathbf{v}_h \qquad \text{in } \Omega \tag{13}$$

where $\mathbf{v}_h$ and $\boldsymbol{\sigma}_h$ represent the discrete counterparts of the fields $\mathbf{v}$ and $\boldsymbol{\sigma}$. In the *weak (strain) discontinuity approach*, the discrete displacement space $\mathbf{u}_h$ consists of polynomial functions inside the elements and interelement continuity is enforced by nodal compatibility; therefore, $\mathbf{u}_h$ is piece-wise continuous. The discrete stress field $\boldsymbol{\sigma}_h$ is a continuous function (through the constitutive equation) of the discrete strain field, $\boldsymbol{\varepsilon}_h = \nabla^s \mathbf{u}_h$, which consists of polynomial functions (of one degree less than the displacements) inside the elements, but is discontinuous at the interfaces between elements. Therefore, strain localization can be *optimally* reproduced by highly localized displacement gradients (strains) across *one single element*.

Solving Eq. (13) is a nonlinear problem because of the dependence of the stresses $\boldsymbol{\sigma}_h$ on the displacements $\mathbf{u}_h$. In practice, this nonlinearity is dealt with assuming that the acting body forces and boundary tractions, $\mathbf{f}$ and $\overline{\mathbf{t}}$, are applied incrementally, being dependent on (pseudo)time or other loading parameter. Then, the problem is solved advancing step-by-step in time (or load), and iterating within each step until equilibrium is satisfied.

4.1.2 Strong (displacement) discontinuity approach

In the strong discontinuity approach ([11], [12], [13], [14], [15]) it is assumed that it exists a material discontinuity $S \subset \Omega$ of zero measure and that discontinuities in the displacement field may occur across S (see Fig. 4). This is the case of a line crack in 2D or a surface crack in 3D.

Note that in the following, the position and extension of the discontinuity S is assumed to be known. The formulation merely states the problem for a given configuration; it is emphasized that, by itself, it does not include any criterion to establish the stability of the crack or to govern its possible extension with time under increasing loading. This has to be derived from different considerations, like bifurcation analysis [13].

The strong form of the continuum mechanical problem can be stated as: find the (discontinuous) displacement field $\mathbf{u}$, for given prescribed body forces $\mathbf{f}$, such that:

$$\nabla \cdot \boldsymbol{\sigma} + \mathbf{f} = \mathbf{0} \qquad \text{in } \Omega \backslash S \qquad (14a)$$
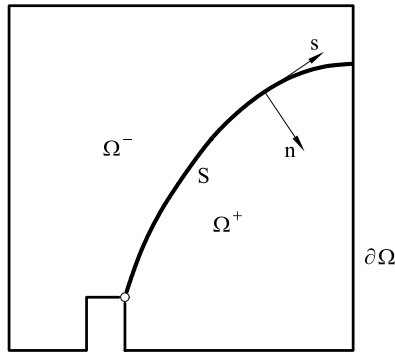$$\mathbf{t}^{\Omega \backslash S} = \mathbf{t}^{S} \qquad \text{in } S \qquad (14b)$$

Figure 4: Strong discontinuity approach

12

where $\Omega \backslash S$ is the part of Ω outside the discontinuity S and $\mathbf{t}$ is the traction vector. Eq. (14a) is subjected to appropriate Diritchlet and Neumann boundary conditions. Note that Eq. (14a) represents internal equilibrium in each one of the two parts, Ω^- and Ω^+, in which S divides Ω; on the other hand, Eq. (14b) represents continuity of tractions across the discontinuity S. It can be observed that these are the same equilibrium equations that govern *contact* between two bodies; kinematic restrictions are also very similar.

Multiplying by the corresponding test functions and integrating by parts the first equation, the associated weak form of the problem can be stated in the form:

$$(\nabla^s \mathbf{v}, \boldsymbol{\sigma}) - (\mathbf{v}, \mathbf{f}) - (\mathbf{v}, \overline{\mathbf{t}})_{\partial \Omega_t} = 0 \qquad \forall \mathbf{v} \qquad \text{in } \Omega \backslash S \qquad (15a)$$

$$\left(\widetilde{\mathbf{v}}, \mathbf{t}^{\Omega \backslash S}\right) - \left(\widetilde{\mathbf{v}}, \mathbf{t}^S\right) = 0 \qquad \forall \widetilde{\mathbf{v}} \qquad \text{in } S \qquad (15b)$$

where $\mathbf{v} \in \mathcal{V}$ are the variations of the continuous part of the displacement field, and $\widetilde{\mathbf{v}} \in \widetilde{\mathcal{V}}$ are the variations of the discontinuous part of the displacement field, $\widetilde{\mathcal{V}} = L^2(S)$. Note that the displacement field $\mathbf{u}$ in Ω can now be discontinuous across S and it can be split as $\mathbf{u} = \bar{\mathbf{u}} + \widetilde{\mathbf{u}}$, where $\bar{\mathbf{u}}$ is continuous in Ω and $\widetilde{\mathbf{u}}$ (some components of it) is discontinuous across S. Eq. (15b) is necessary to determine $\widetilde{\mathbf{u}}$.

The corresponding discrete problem is

$$(\nabla^s \mathbf{v}_h, \boldsymbol{\sigma}_h) - (\mathbf{v}_h, \mathbf{f}) - (\mathbf{v}_h, \overline{\mathbf{t}})_{\partial \Omega_t} = 0 \qquad \forall \mathbf{v}_h \qquad \text{in } \Omega \backslash S \qquad (16a)$$

$$\left(\widetilde{\mathbf{v}}_h, \mathbf{t}_h^{\Omega \backslash S}\right) - \left(\widetilde{\mathbf{v}}_h, \mathbf{t}_h^S\right) = 0 \qquad \forall \widetilde{\mathbf{v}}_h \qquad \text{in } S \qquad (16b)$$

where $\mathbf{v}_h, \widetilde{\mathbf{v}}_h$ and $\boldsymbol{\sigma}_h, \mathbf{t}_h$ represent the discrete counterparts of the fields $\mathbf{v}, \widetilde{\mathbf{v}}$ and $\boldsymbol{\sigma}, \mathbf{t}$. In the *strong discontinuity approach*, several possibilities appear when defining the spatial discretization of the displacement field. One of them is to use finite elements with *embedded discontinuities*. Here, the elements crossed by the discontinuity, *and only them*, are enriched with additional degrees of freedom to parametrize the discontinuous part $\widetilde{\mathbf{u}}$. Precisely, Eq. (16b) is necessary to determine these additional dofs. Therefore, the discrete displacement space $\mathbf{u}_h$ is piece-wise continuous in $\Omega \backslash S$, but discontinuous across S. The discrete strain field $\boldsymbol{\varepsilon}_h$ consists of polynomial functions (of one degree less than the displacements) inside the elements and discontinuous at the interfaces between elements in $\Omega \backslash S$, but grows to infinity across S. Figure 3b shows this situation.

Solving Eqs. (16a)-(16b) is obviously a nonlinear problem. As in the weak discontinuity approach, this nonlinearity is dealt with advancing step-by-step in time (or load), and iterating within each step until the required equations are satisfied.

4.2   Stability of the weak and strong discontinuity approaches

The governing Eqs. (11) and (14a), stated in terms of the *total* displacement $\mathbf{u}$ (not the *rate* equations, written in terms of the *incremental* displacements), can be rewritten in terms of the deviatoric and volumetric parts of the deformation as

$$\nabla \cdot (G \nabla^s \mathbf{u}) + \nabla (K \nabla \cdot \mathbf{u}) + \mathbf{f} = \mathbf{0} \qquad \text{in } \Omega \qquad (17)$$

where G and K are the shear and bulk moduli, respectively.

A standard stability (or energy) estimate for problem (17) is obtained by multiplying the first two terms of the left hand side by $\mathbf{u}$ and integrating by parts over the domain Ω, to yield

$$(\nabla^s \mathbf{u}, G \nabla^s \mathbf{u}) + (\nabla \cdot \mathbf{u}, K \nabla \cdot \mathbf{u}) = \|\mathbf{u}\|_E^2 > 0 \qquad (18)$$

where $\|\cdot\|_E^2$ is the energy norm (equal to the elastic free energy). Therefore, the governing equations for the weak and strong discontinuity approaches are stable, for strictly positive elastic moduli, $G, K > 0$. This means that the solution $\mathbf{u}$ can be bounded, in this case in the energy norm, in terms of the data.

For an isotropic damage model, the stability estimate reads

$$(\nabla^s \mathbf{u}, G_{\text{sec}} \nabla^s \mathbf{u}) + (\nabla \cdot \mathbf{u}, K_{\text{sec}} \nabla \cdot \mathbf{u}) > 0 \qquad (19)$$

where stability of the problem can be guaranteed as long as the *secant* moduli, $G_{\text{sec}} = (1 - d)G$ and $K_{\text{sec}} = (1 - d)K$, remain strictly positive, that is, for damage index $d < 1$. Eq. (19) still holds if the secant moduli vanish completely ($d = 0$) only in a subdomain $S \subset \Omega$ of zero measure. Conversely, the problem becomes unstable if there are subdomains of non-zero measure in Ω which lose the stiffness completely.

Regarding the discrete problem, the same restrictions apply for the governing equation to be stable,

$$(\nabla^s \mathbf{u}_h, G_{\text{sec}} \nabla^s \mathbf{u}_h) + (\nabla \cdot \mathbf{u}_h, K_{\text{sec}} \nabla \cdot \mathbf{u}_h) > 0 \qquad (20)$$

where $\mathbf{u}_h$ represents the discrete displacement field. It would seem that stability can only be maintained if $\mathbf{u}_h$ is discontinuous (strong discontinuity), ensuring that the secant moduli vanish completely only in a subdomain of zero measure in Ω. However, and having standard finite element discretizations in mind, we can admit that the problem remains stable if the secant moduli vanish only in a properly restricted subdomain in Ω, such as in a band of elements (one element across) overlapping the crack. This opens the possibility of solving crack propagation problems using standard elements with continuous displacement fields $\mathbf{u}_h$ (weak discontinuity), if the extension of the totally damaged areas is restricted to a band one element across.

5   The problem of crack propagation

5.1   Local approximation error

In fracture mechanics, the two basic ingredients of the physical model are: (a) the criterion for crack *propagation* (instability), which is usually established in terms of the stored elastic energy, and (b) the criterion for selecting the *direction* of crack propagation, which is established empirically among several possibilities [32]. Once these two ingredients are established, the problem of crack propagation is invariably tackled in a staggered, two stage, procedure: for a *given crack configuration*, (i) solve the mechanical problem in order to compute the stress field and, consequently, to determine if the crack is unstable and (ii) if so, update the crack path, by advancing the crack tip a small distance, according to the selected criterion for crack propagation. Necessarily, crack tracking algorithms are always an essential part of fracture mechanics based codes, and are also crucial in the application of the X-FEM.

In a continuum mechanics framework, the same procedure can be hypothetically followed, now involving: for a *given damage distribution*, (i) solve the mechanical problem in order to compute the stress field Eq. (13) and, consequently, (ii) update the damage distribution. This second stage involves two different operations: (ii.a) to update the damage index in those elements previously damaged and (ii.b) to decide which elements are newly damaged.

Observe now the implications of proceeding in this way. Stage (i) consists of solving a *linear elastic* BVP, with a *given distribution of (positive) elastic moduli*. The problem is obviously *linear, well posed, elliptic, stable* and the solution is *unique*. Note also that while solving this problem it is never

necessary to evaluate any negative *tangent* elastic modulus. Stage (ii.a) is trivial, as damage is an explicit function of the strain history. Stage (ii.b), deciding which elements are newly damaged, requires some more deliberation.

In the classical smeared crack approach it has always been implicitly understood that the criterion for the onset of cracking, which is always established in terms of stresses/strains, also must *automatically* define the direction of propagation. This is a natural assumption in the continuum problem, with proper evaluation of stress and strain values and directions. However, in the discrete problem the stress and strain fields evaluated in the vicinity of the crack tip differ greatly from being exact. As a consequence, the automatic application of the cracking criterion for the evaluation of the direction of crack growth leads to an unacceptable dependence on the mesh bias in this region.

This local approximation error due to the spatial discretization in the vicinity of the crack tip is the main difficulty to be overcome when solving the problem of tensile crack propagation. In fracture mechanics, this was traditionally solved by the use of special finite elements in the discretization of this region (see reference [7]). More recently, the X-FEM applied to LEFM problems proves effectively that mesh bias is eliminated if the functional space of the discrete displacement field is enriched with functions that contain the *analytical solution* in the vicinity of the crack tip ([8], [9], [10]).

The same situation arises in continuum mechanics: remarkably, and although it is not always explicitly stated, all successful applications of the strong discontinuity approach use tracking algorithms to lead the direction of crack propagation. In fact, Mosler and Meschke [18] have proved that if tracking is not used, the strong discontinuity formulation leads to the same spurious mesh bias dependence as the standard weak discontinuity approach. On the other hand, Grassl and Jirásek [33] have reported that tracking techniques substantially improve the results obtained with local damage models.

All this evidence points to the conclusion that solving in an adequate manner the problem of crack propagation is essential also in a continuum framework of the crack growth problem, *both* if continuous or discontinuous displacement fields are used in the interpolation basis.

5.2   Evaluation of the propagation direction

In this work we will explicitly consider the evaluation of the propagation direction as a separate problem, obviously coupled to that of solving the

equilibrium equation (13). This evaluation must be *consistently linked* to the cracking criterion, as this is the established cracking mechanism at continuum level, and it cannot be *locally dependent* on the discrete stress/strain fields, as these may be substantially off-track.

For a Rankine damage criterion, let us assume that the crack propagates following a surface (a line in 2D) which is orthogonal to the direction of the maximum positive principal stress. Then, to be able to predict the direction of propagation of the crack it is necessary to evaluate the *principal stress trajectories* in the vicinity of the crack tip. Therefore, what is needed is a procedure capable of accurately computing these trajectories in the region of interest. The following procedure was proposed in reference [14] in the strong discontinuity framework, and it has been already applied in 2D and 3D applications [16].

Let $\mathbf{n}$ be a field of unit vectors in the direction of the maximum positive principal stress at each point of the domain, and $\mathbf{s}$ and $\mathbf{t}$ be any two orthogonal unit vectors orthogonal to it. Let θ be a scalar field such that its gradient is parallel to the given vector field $\mathbf{n}$, so that $\mathbf{n} = \nabla\theta\,/\,\|\nabla\theta\|$. It is clear that the iso-level surfaces (lines in 2D) defined by $\theta = cte$ are orthogonal to $\mathbf{n}$. Therefore, the crack propagates along one particular iso-level surface S defined by $\theta = \bar{\theta}_o$. Thus, the problem of evaluating the direction of crack propagation is equivalent to finding the scalar field θ and determining the iso-level locus $\theta = \bar{\theta}_o$.

This is conveniently formulated as the following *linear* BVP: find the scalar field θ, such that:

$$\nabla \cdot (\mathbf{K} \cdot \nabla\theta) = 0 \qquad \text{in } \Omega \tag{21}$$

where Ω is the open and bounded domain of $\mathbb{R}^{n_{\dim}}$ occupied by the solid in a space of $n_{\dim}$ dimensions.

Eq. (21) is subjected to appropriate boundary conditions. Let $\mathbf{x}_o$ be the point of the boundary where the crack is initiated and $\bar{S} \subset S$ be the part of the surface S where the cracking criterion has already been violated (consolidated part of the crack). Dirichlet boundary conditions are specified in (a) a part of the boundary $\partial\Omega_\theta \subset \partial\Omega$ including the seminal point $\mathbf{x}_o \in \partial\Omega_\theta$, and so that $\theta(\mathbf{x}_o) = \bar{\theta}_o$ and (b) along $\bar{S}$, so that $\theta(\mathbf{x}) = \bar{\theta}_o$ for points $\mathbf{x} \in \bar{S}$; natural boundary conditions are imposed elsewhere at $\partial\Omega$ (see Fig. 5).

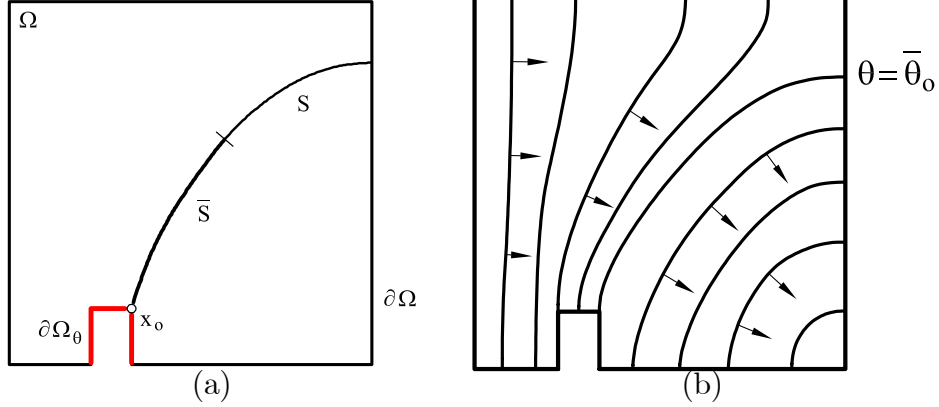The second-order tensor $\mathbf{K}$ couples the scalar problem (21) to the evolu-

Figure 5: Tracking algorithm: (a) definition, (b) iso-level curves

tion of the mechanical problem, Eq. (11). It takes the form

$$\mathbf{K} = \mathbf{t} \otimes \mathbf{t} + \mathbf{s} \otimes \mathbf{s} + \varepsilon \, \mathbf{n} \otimes \mathbf{n} \tag{22}$$

where ε is a small perturbation value, $\varepsilon = 10^{-4} \div 10^{-10}$. This enforces that $\mathbf{n} = \nabla\theta \, / \, \|\nabla\theta\|$.

Note that, in these conditions, the size of $\partial\Omega_\theta$, the part of the boundary where θ is prescribed and the actual values of θ used in the prescription need not be uniquely defined, as the trajectory of the iso-line starting at $\mathbf{x}_o$ will not be effectively affected by these parameters. Typically, let us take $\partial\Omega_\theta$, see Fig. 5, as the inside boundary of the notch we want to investigate, and let θ vary linearly along it with an arbitrary gradient but satisfying $\theta\left(\mathbf{x}_o\right) = \bar{\theta}_o$.

The associated weak form of the problem can be stated as:

$$(\mathbf{K} \cdot \nabla\theta, \nabla\eta) = 0 \qquad \forall\eta \tag{23}$$

where $\eta \in \mathcal{Q} = H^1\left(\Omega\right)$ are the variations of the scalar field, and $(\cdot, \cdot)$ denotes the inner product in $L^2\left(\Omega\right)$. The corresponding discrete problem is

$$(\mathbf{K} \cdot \nabla\theta_h, \nabla\eta_h) = 0 \qquad \forall\eta_h \tag{24}$$

where θ_h and η_h are the discrete counterparts of θ and η. In the discrete problem, when the smeared crack approach is adopted, the elements crossed by the iso-surface (or line) $\theta = \bar{\theta}_o$ are assumed to belong to the locus S. Therefore, the corresponding boundary condition is imposed at the nodes pertaining to those elements.

18

Problem (24) is very simple, as it is linear, elliptic and it only involves one unknown per node. Besides, being a conduction-like problem, it is sufficiently well-behaved and it does not present any singular point in the vicinity of the advancing crack. It can be solved using the same FE mesh as problem (13) and the coupling with it can be enforced once per time increment or, more rigorously, at each iteration. Once it is solved, and the elements e lying along the iso-level locus S, such that $\theta = \bar{\theta}_o$, are identified, these are subsequently known to the mechanical solver when performing the check on the crack criterion; only those elements crossed by S are allowed to crack, and those actually cracked are added to the consolidated part of the track $\bar{S} \subset S$.

The described algorithm can be easily extended to track the propagation of multiple cracks, simply by defining the $i - th$ crack as the locus S^i where $\theta = \bar{\theta}_o^i$ and specifying the corresponding boundary conditions at $\bar{S}^i \subset S^i$. The case of intersecting cracks, however, cannot be as easily accommodated in this procedure.

6 Numerical examples

The formulation presented in the preceding sections is illustrated below by solving three benchmark problems. Performance of the standard continuous displacement (weak discontinuities) finite elements is tested considering standard *2D plane-stress 3-noded linear triangular* meshes.

The examples are solved using the isotropic damage model presented in Section 3 with exponential *strain softening*, regularized according to the element size, and the global tracking algorithm presented in Section 5.

The discrete weak form of the mechanical problem is solved incrementally, in a (pseudo)time step-by-step manner. In all cases 200 equal time steps are performed to complete the analyses. Within each step, a modified Newton-Raphson method (using the secant stiffness matrix), together with a line search procedure, is used to solve the corresponding non-linear system of equations. Convergence of a time step is attained when the ratio between the iterative and the incremental norm of the computed displacements is lower than 10^{-3} (0.1 %).

Calculations are performed with an enhanced version of the finite element program COMET [34], developed by the authors at the International Center for Numerical Methods in Engineering (CIMNE). Pre and post-processing is done with GiD, also developed at CIMNE [35].

6.1 Double edge notched specimen (DENS)

This example is selected because it corresponds to a series of tests fully documented in Nooru-Mohamed's Doctoral Thesis [36] and it has been numerically simulated in many occasions using different crack approaches ([14], [17], [37], [38]).

The specimen is square shaped and double edge notched (DENS), with dimensions $200 \times 200 \times 50$ mm^3, and notch depths of 25 mm and widths of 5 mm. A schematic diagram of the geometry of the specimen and the testing arrangement is shown in Figure 6.

The experiments were designed to subject the specimen to mixed-mode tensile cracking. The DENS was placed in a special rigid loading frame to allow for the analysis of various loading paths combining shear and tension under force and/or displacement control. The specimen to be studied here was supported at the bottom and along the right-hand side below the notch. The shear force P_s was applied through the frame along the left-hand side of the specimen above the notch and the normal force P was applied at the top. The frames were glued to the specimen. The relative normal deformation in the fracture zone δ was measured between the points marked in the sketch,
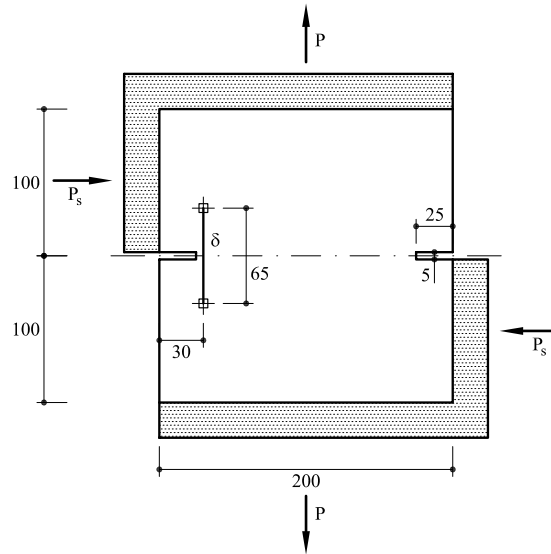

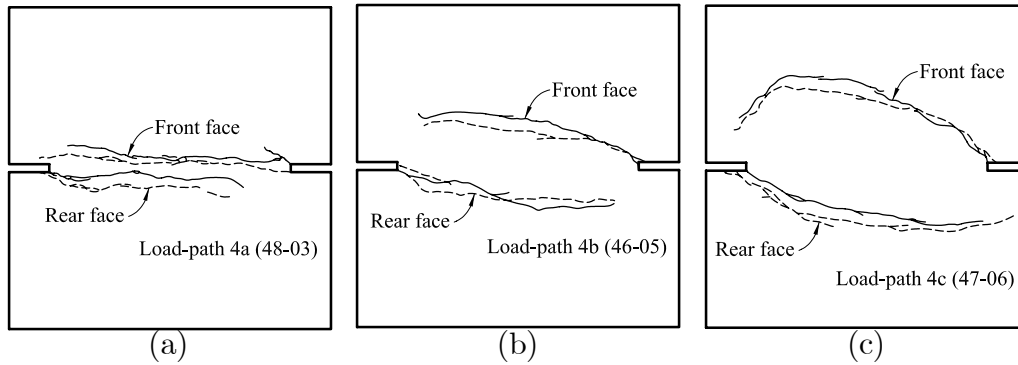Figure 6: Geometry and load for double edge notched specimen (DENS)

20

Figure 7: Experimentally obtained crack patterns for double edge notched specimen s

65 mm apart and 30 mm from the left-hand side boundary.

Three different load-paths are investigated here, 4a 48-03, 4b 46-05 and 4c 47-06. They are characterized by different values of the firstly applied shear force P_s (while $P = 0$): 5 kN for DENS-4a, 10 kN for DENS-4b and $P_s^{\max} = 27.5$ kN for DENS-4c. The experiment continues by keeping the applied shear force P_s constant, while progressively increasing the axial vertical displacement. The corresponding normal reaction P is measured throughout the experiment.

Figure 7 shows the crack patterns obtained in the experiments. It should be observed that, although very interesting, these experimental results cannot be accepted unquestionably. First, the difference in cracking between the front and the rear faces indicates that the specimens were not really tested under pure membrane action, some bending may have spuriously happened. Furthermore, the cracks at the top and bottom of the specimens do not show the symmetry that would be expected from the intended boundary conditions. This may be due to a number of reason dealing with the set up of the fixings. Anyhow, they are affecting the strain/stress field in at least one half of the specimens significantly. Other comment is that it was reported that the frame and the specimens, although being glued, suffered separation in some cases, particularly at the top-right and bottom-left corners, where some spurious cracking was observed in some specimens. Also, it is worth to mention that all the numerical simulations referred to these tests tend to evaluate peak values for the normal forces P which are overestimated when compared to the experimental values. This may be due to the mentioned de-

ficiencies in the experimental set up. Finally, the specimens were of different ages in the moment of their testing. All this means that the confidence on the experimental results must be critically evaluated.

The computational domain is discretized in two different unstructured meshes of *2D plane-stress 3-noded linear triangular elements* with average mesh sizes of $h_e = 5$ mm (2,125 nodes) and $h_e = 2.5$ mm (8,391 nodes). Although this may seem a very refined degree of discretization, it must be observed that the difference in the global elastic stiffness under the shear forces is 7 % between the "coarse" and "fine" meshes, the latter being obviously smaller. This is because of the presence of the two notches, which render the nearby areas nearly singular. Regarding the computational boundary conditions, they have been defined exactly symmetrical, with the central node of the mesh being fixed in the horizontal and vertical dofs.

For each of the load-paths, four different analyses have been performed: (a.1) coarse mesh with tracking, (a.2) coarse mesh without tracking, (b.1) fine mesh with tracking and (b.2) fine mesh without tracking. The pre-processor used tends to introduce patches of equilateral triangles with predominant directions at -60°, 0° and $+60^o$ with the horizontal axis, particularly for the finer mesh. The results obtained are discussed in the following.

6.2   Load path 4a

For load-path 4a (specimen 48-03) the loading is applied in two stages: first, a shear force $P_s = 5$ kN is applied, while keeping the normal force $P = 0$; later, the experiment continues by keeping the applied shear force P_s constant, while progressively increasing the axial vertical displacement Δ.

The following material properties are assumed for this case: Young's modulus $E = 30$ GPa, Poisson's ratio $\nu = 0.2$, tensile strength $\sigma_o = 2.8$ MPa and mode I fracture energy $G_f = 90$ J/m^2.

As commented, four separate analyses are performed using th two meshes. The computed deformed shapes of the specimen are shown in Figures 8a and 8b, for the coarse and fine meshes, respectively (imposed total vertical displacement $\Delta = 0.2$ mm, with a displacement amplification factor of 100). The different element sizes in the meshes can be appreciated in these figures. As shown, the computed cracks in the two analyses where tracking was performed (top figures) follow very closely the same path, starting at the tip of the notches and tilting slightly due to the orientation of the strain field. No spurious mesh bias is observed in any of these analyses.
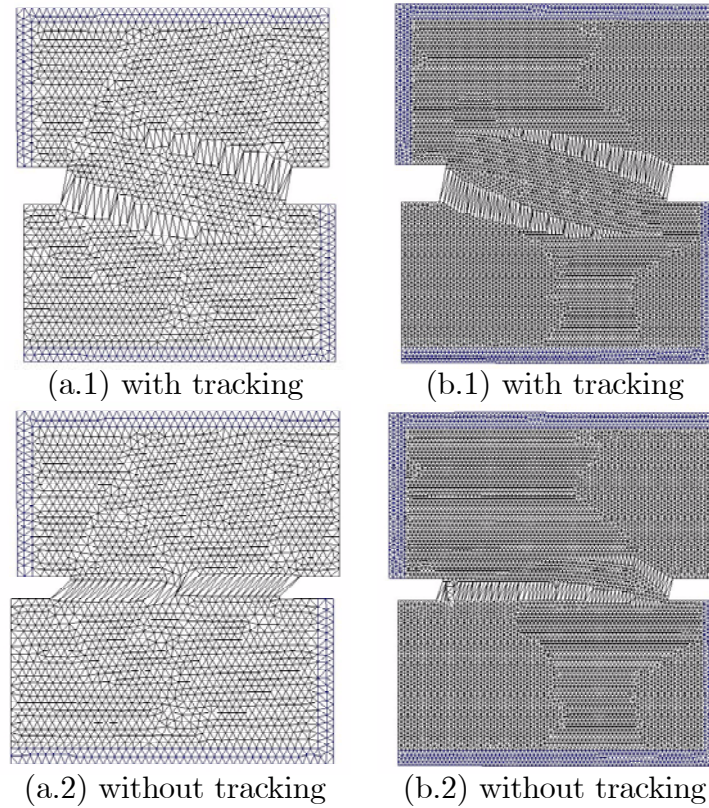
(a.1) with tracking   (b.1) with tracking

(a.2) without tracking   (b.2) without tracking

Figure 8: Deformed geometries (x 100) on the two meshes with and without tracking for double edge notched specimen - load path 4a

If no tracking strategy is used, see Figures 8a.2 and 8b.2, the cracks initiate correctly, but they turn horizontally almost immediately to run along with the respective mesh alignment and too close to the horizontal axis.

Figure 9 shows load vs imposed vertical displacement curves obtained with the two different meshes, and using tracking. In this example the loading branch curves slowly as the cracks progress, turning into the softening branch once the failure mechanism is fully developed. Load does not vanish completely because only damage due to tensile effective stresses is considered, and the state of stresses near the opposite notch is mostly compressive.

Note that the overall global response is very similar upon mesh refinement, although the effect of the different spatial discretizations can be observed even in the global elastic stiffness of the specimen. This shows that solving problems involving singular stress points requires a high level of resolution.
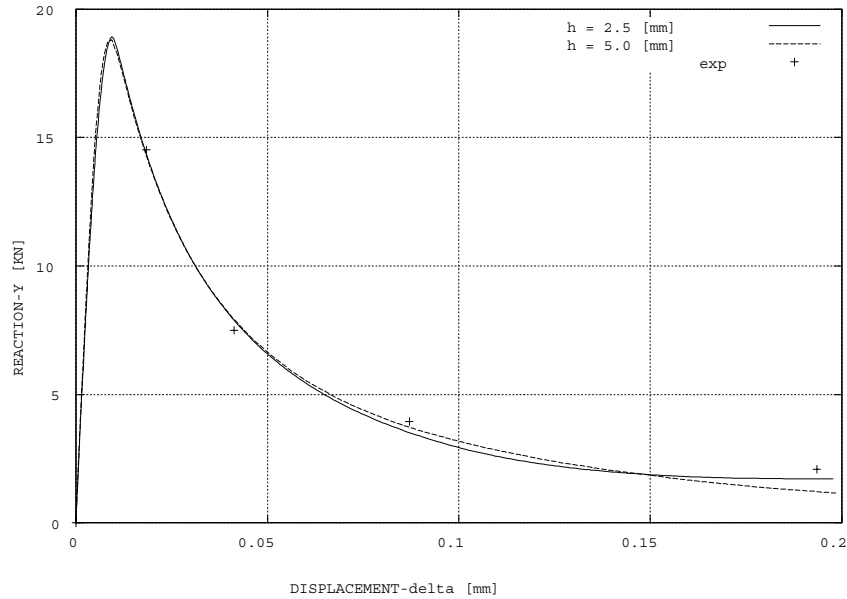
Figure 9: Load *versus* displacement for double edge notched specimen - load path 4a. Comparison between different mesh sizes

No spurious brittleness is observed when the size of the elements in the mesh is reduced.

Figure 10 shows the results obtained using the proposed formulation on the fine mesh. The three columns represent, respectively, the evolution, at three different time steps of the analysis, of: (a) the contours of total displacements, (b) the contours of the damage index and (c) the maximum principal strain vectors. The progressive concentration of the displacement gradients (strains) in the elements along the crack paths is evident in the three columns. The bottom figures show how, when the failure mechanism is fully developed, all the deformation concentrates in the formed cracks, while the elements outside these bands are mostly undeformed. Note that the resolution of the cracks is optimal for the mesh used. Observe in the left bottom plot how, once both cracks are formed, the central part of the specimen rotates almost as a rigid body around the center of the specimen. For the coarser mesh, similar results are obtained, although the strain localization is smeared across a row of larger elements (see Fig. 8).

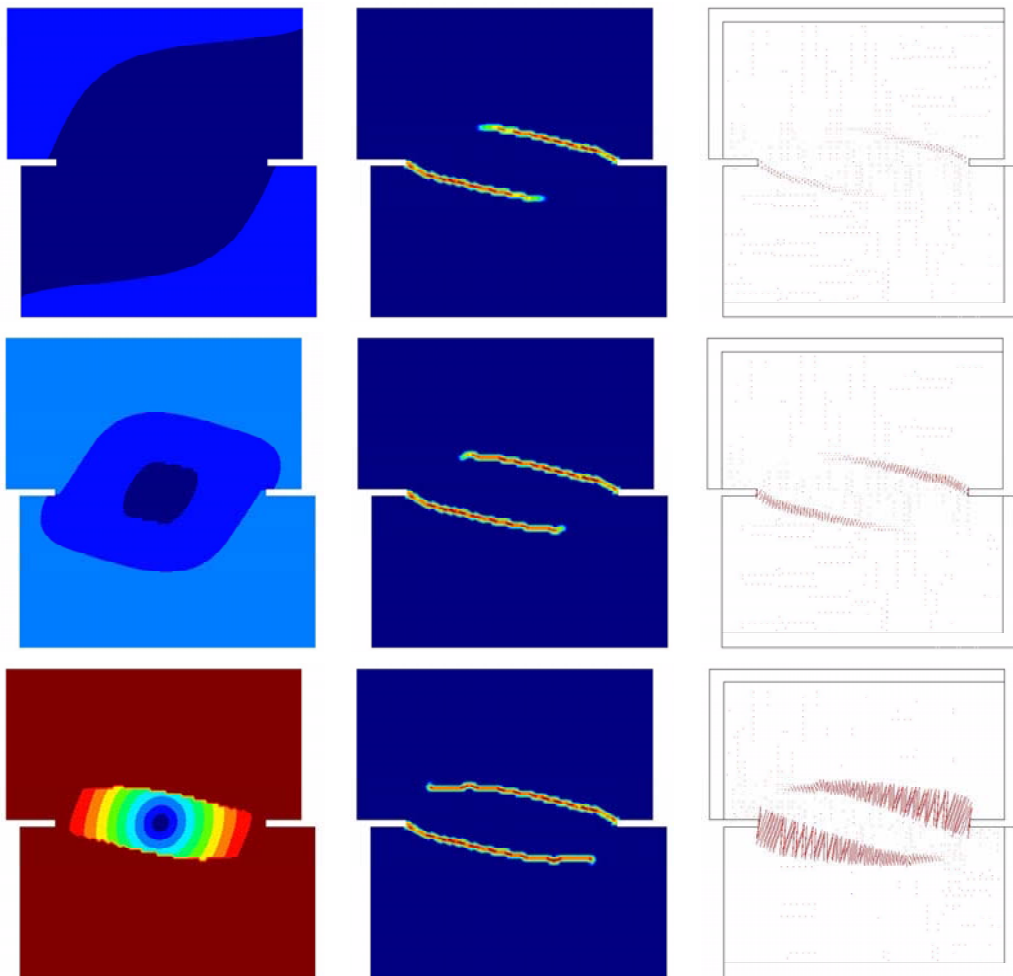In the third column, it can be observed that, although this experiment has

24

Figure 10: Results for double edge notched specimen (load path 4a). Evolution of: (a) displacement, (b) damage, (c) vectors of max. principal strain

been devised as a mixed-mode cracking test, and the cracks indeed initiate at an angle from the notches, the failure mechanism is mainly in pure mode I, as the computed maximum tensile principal strain vectors (as the related vectors of maximum tensile principal effective stress) are mostly orthogonal to the crack path. Note also that the correct failure mechanism has been predicted although the directions of some of the computed maximum principal strain vectors are clearly dependent on the mesh bias, as they are not orthogonal to the crack path everywhere.

25

Figure 11: Evolution of the profiles along the central vertical axis of: (a) vertical displacement and (b) maximum principal strain for double edge notched specimen (load path 4a)

Finally, Figures 11a and 11b show the evolution, at three different time steps of the analysis, of: (a) the vertical displacement and (b) the maximum principal strain, along a vertical line along the centre of the specimen which crosses both cracks. In these, it can be observed how the initially smooth gradient of displacements progressively localizes into two very sharp (but weak) jumps across one single element. Also, the strain profile progressively localizes with very sharp resolution of the two (weak) discontinuities formed. It is therefore shown that, in practice, there exists little difference between a

highly resolved weak discontinuity and a strong discontinuity.

6.3   Load path 4b

For load-path 4b (specimen 46-05) the loading is also applied in two stages: first, a shear force $P_s = 10$ kN is applied, while keeping the normal force $P = 0$; later, the experiment continues by keeping the applied shear force P_s constant, while progressively increasing the axial vertical displacement Δ.

The following material properties are assumed for this case: Young's modulus $E = 30$ GPa, Poisson's ratio $\nu = 0.2$, tensile strength $\sigma_o = 2.2$ MPa and mode I fracture energy $G_f = 80$ J/m^2.

Again, four separate analyses are performed using the two different meshes. The computed deformed shapes of the specimen are shown in Figures 12a

(a.1) with tracking   (b.1) with tracking

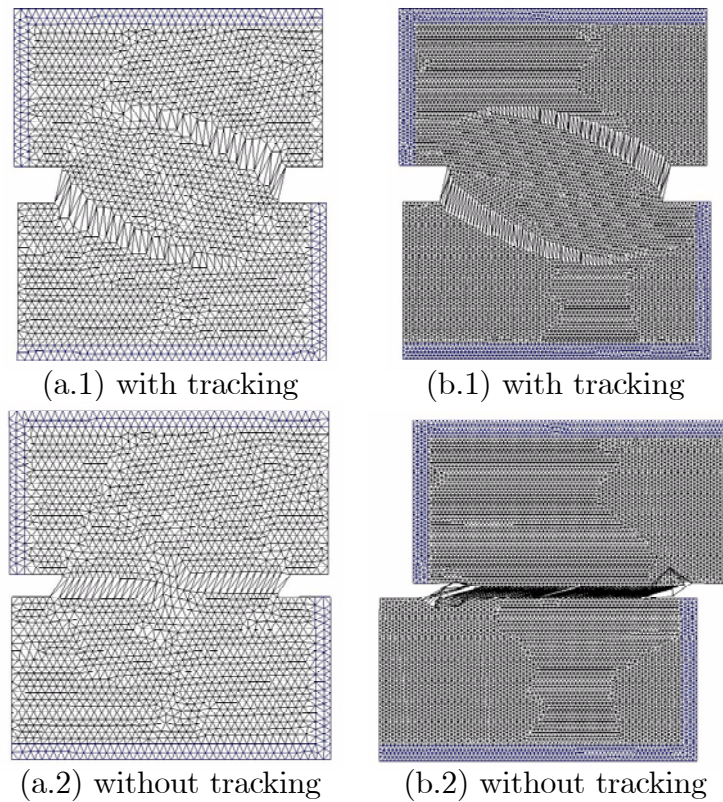(a.2) without tracking   (b.2) without tracking

Figure 12: Deformed geometries (x 100) on the two meshes with and without tracking for double edge notched specimen (load path 4b)

and 12b, for the coarse and fine meshes, respectively (imposed total vertical displacement $\Delta = 0.2$ mm, with a displacement amplification factor of 100). As shown, the computed cracks in the two analyses where tracking was performed (top figures) follow very closely the same path, and no spurious mesh bias is observed in any of these analyses. The elevation that the top crack reaches above the horizontal axis matches almost exactly that observed in the experiment (see Fig. 7b).

If no tracking strategy is used, see Figures 12a.2 and 12b.2, the cracks are practically horizontal, running along with the mesh alignment and practically coinciding with the horizontal axis. The analysis on the fine mesh fails along this axis at a much earlier stage than expected.

Figure 13 shows load vs imposed vertical displacement curves obtained with the two different meshes, and using tracking. In this example the loading branch curves more slowly as the cracks progress, turning into the softening branch once the failure mechanism is fully developed. Load almost vanishes completely at the end of the analyses. As in the previous example, the
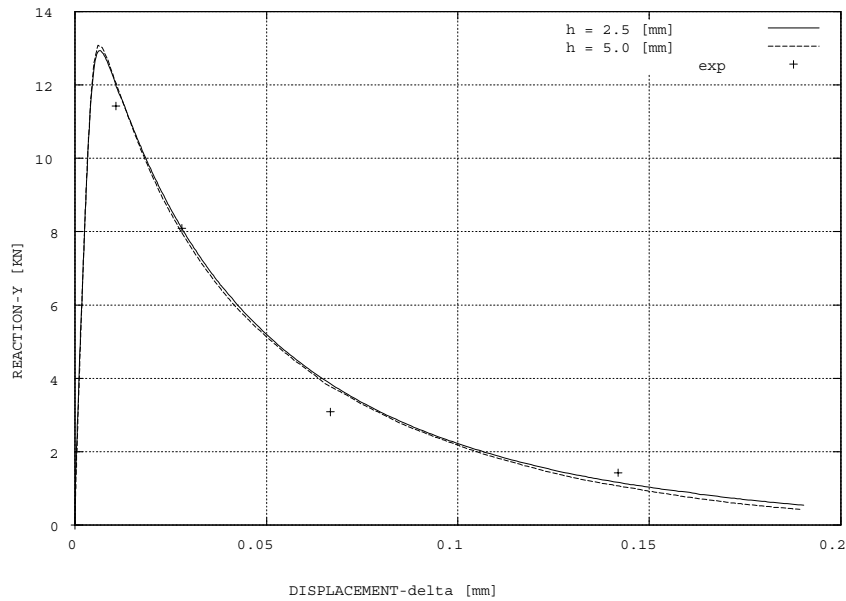

Figure 13: Load *versus* displacement for double edge notched specimen - load path 4b. Comparison between different mesh sizes
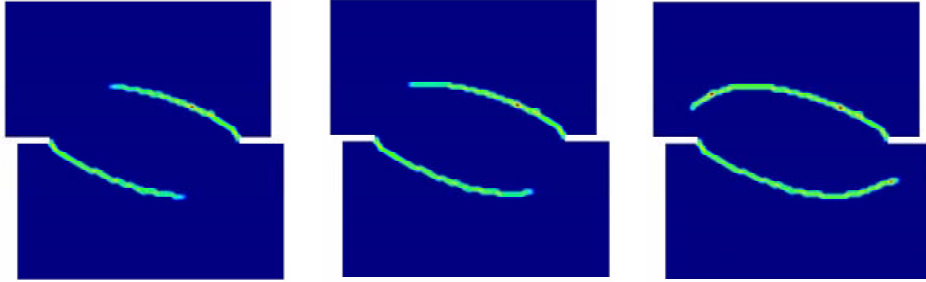
28

Figure 14: Evolution of damage index for double edge notched specimen (load path 4b)

overall global response is very similar upon mesh refinement, and no spurious brittleness is observed when the size of the elements in the mesh is reduced.

Figure 14 shows the evolution of the damage obtained using the proposed formulation on the fine mesh.

6.4 Load path 4c

For load-path 4c (specimen 47-06) the loading is also in two stages: first, the maximum shear force that the specimen can sustain, $P_s^{\max} = 27.5$ kN, is applied, while keeping the normal force $P = 0$; later, the experiment continues by keeping the applied shear force $P_s^{\max}$ constant, while progressively increasing the axial vertical displacement Δ.

The following material properties are assumed for this case: Young's modulus $E = 30$ GPa, Poisson's ratio $\nu = 0.2$, tensile strength $\sigma_o = 2.2$ MPa and mode I fracture energy $G_f = 80$ J/m^2.

As commented, four separate analyses are performed using the coarse and fine meshes. In the FE analyses, the maximum shear force sustained by the coarse mesh was $P_s^{\max} = 27.5$ kN, but the fine mesh sustained a slightly higher shear force of $P_s^{\max} = 28.6$ kN (6 % higher) to reach the same state of crack propagation. This is due to the 7 % difference in the global stiffness of the two meshes. This explains the differences observed in the corresponding responses during the later stage of axial straining.

The computed deformed shapes of the specimen are shown in Figures 15a and 15b, for the coarse and fine meshes, respectively (imposed total vertical displacement $\Delta = 0.2$ mm, with a displacement amplification factor of 100). As shown, the computed cracks in the two analyses where tracking

(a.1) with tracking   (b.1) with tracking

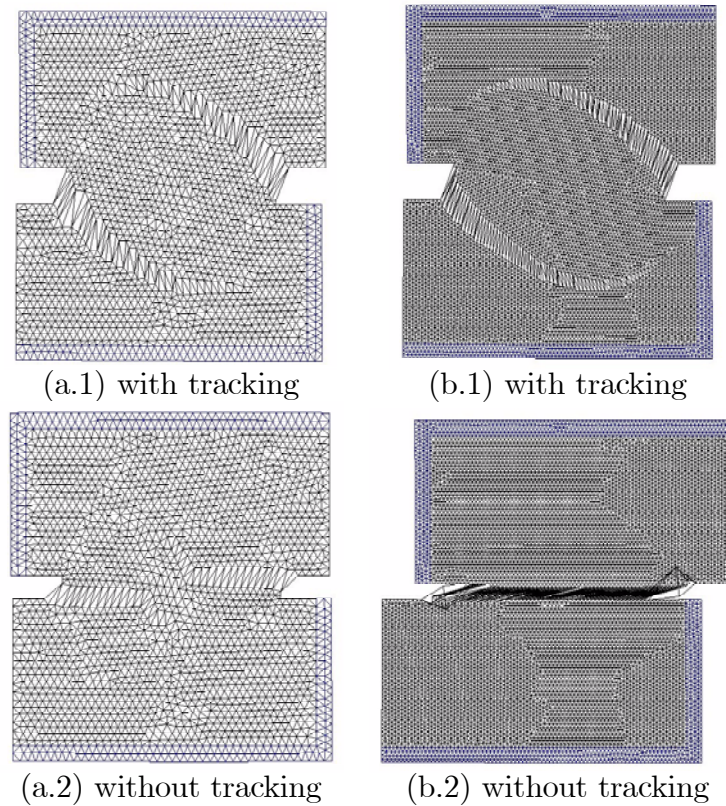(a.2) without tracking   (b.2) without tracking

Figure 15: Deformed geometries (x 100) on the two meshes with and without tracking for double edge notched specimen (load path 4c)

was performed (top figures) follow very closely the same path, starting at the tip of the notches and progressively curving inwards due to the reorientation of the strain field. Agreement with the experimental pattern (see Fig. 7c) is remarkable. No spurious mesh bias is observed in any of these analyses.

If no tracking strategy is used, see Figures 15a.2 and 15b.2, the cracks form almost horizontally, in a totally unrealistic manner. As in the previous example, the analysis performed with the fine mesh fails prematurely.

Figure 16 shows load vs imposed vertical displacement curves obtained with the two different meshes, and using tracking. This graph is surprising, as it shows that the axial force P turns rapidly to be negative, even if the applied axial displacement is positive, corresponding to pulling apart the fixing frames. Only reference [38] reports success in modelling this curious result, while reference [37] clearly states that the model used there cannot
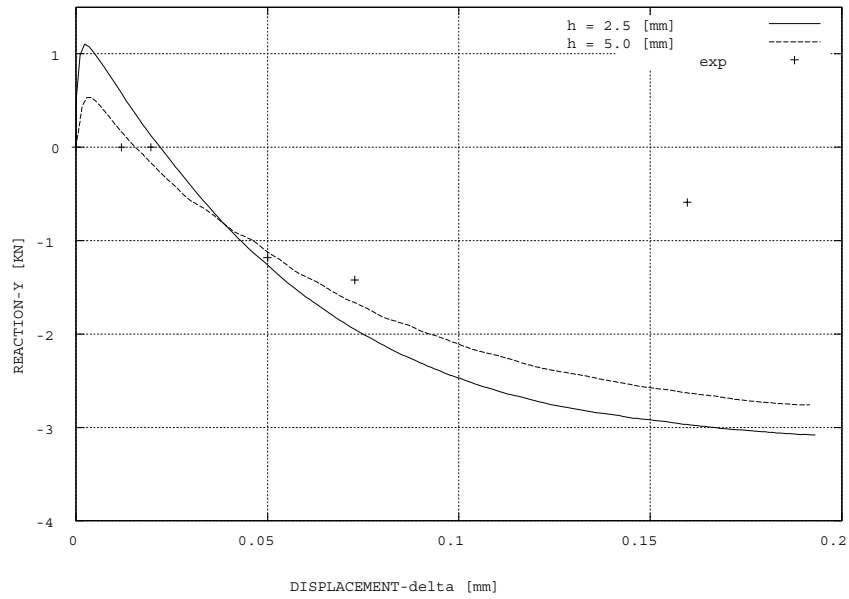
Figure 16: Load *versus* displacement for double edge notched specimen - load path 4c. Comparison between different mesh sizes

reproduce this compressive state. Note that the value of the normal forces P involved in this case is much lower than the shear forces $P_s^{\max}$. This explains the relative difference in the results obtained with the two meshes.

Finally, Figure 17 shows the evolution of the damage index obtained using the proposed formulation on the fine mesh.
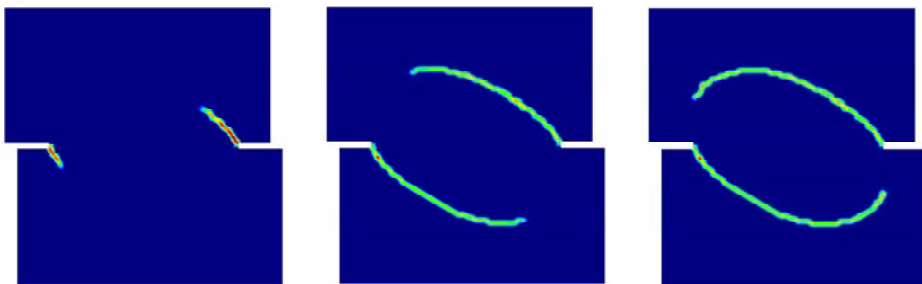

Figure 17: Evolution of the damage index for double edge notched specimen (load path 4c)

7   Conclusions

This paper shows the application of *standard finite elements* with continuous displacement fields, such as linear triangles, to the solution of problems involving the propagation of tensile cracks using the classical smeared crack approach, in this case, via a *local* isotropic continuum damage model with strain softening regularized using the classical *fracture energy regularization technique.*

The main novelty of the paper is to consider the determination of the direction of propagation of the strain localization band as a separate problem, coupled to that of solving the equation of equilibrium. The necessity of doing this stems from previous experience with the discrete crack approach, both in the *fracture* and *continuum* mechanics frameworks, but also from the stability analysis of the weak forms of the associated mechanical problem, both in continuum and discrete formats.

A mesh objective formulation of the problem is obtained, which translates in the achievement of two goals: (1) the position and orientation of the localization paths (cracks) are independent of the directional bias of the finite element mesh, and (2) the global post-peak load-deflection curves are independent of the size of the elements in the localization path (crack).

Numerical examples show, on one hand, the advantage of using a crack propagation algorithm to predict correct failure mechanisms with localized patterns of tensile deformation, virtually free from any dependence of the mesh directional bias; on the other, these techniques are shown to produce results which exhibit the correct amount of dissipated energy during the localization (fracture) process, directly related to the fracture energy of the material, yielding a correct global response in the softening regime. Finally, computed solutions show that, as expected, the weak discontinuity concept converges upon mesh refinement to the strong discontinuity approach.

References

[1] Cervera, M., Chiumenti, M. and Agelet de Saracibar, C. 2003. Softening, localization and stabilization: capture of discontinuous solutions in J2 plasticity. Int. J. for Num. and Anal. Meth. in Geomechanics, 28, 373-393.

[2] Cervera, M., Chiumenti, M. and Agelet de Saracibar, C. 2003. Shear band localization via local J_2 continuum damage mechanics. Comp. Meth. in Appl. Mech. and Eng., 193, 849-880.

[3] Clough, R.W. (1962). The stress distribution of Norfolk Dam. Structures and Materials Research, Department of Civil Engineering Series 100, 19, University of California, Berkeley, California, USA.

[4] Ngo, D. and Scordelis, A.C. (1967). Finite element analysis of reinforced concrete beams. ACI Journal, 64(14), 152-163.

[5] Nilson, A.H. (1968). Nonlinear Analysis of Reinforced Concrete by the Finite Element Method. ACI Journal, 65(9), 757-776.

[6] Tong, P. and Pian, T.H.H. (1973). On the convergence of the finite element method for problems with singularily. Int. J. Solids struct., 9, 313-321.

[7] Owen, D.R.J. and Fawkes, A.J. (1983). Engineering Fracture Mechanics, Pineridge Press, Swansea.

[8] Belytschko, T. and Black, T. (1999). Elastic crack growth in finite elements with minimal remeshing. Comp. Meth. in Appl. Mech. and Eng., 45(5), 601-620.

[9] Möes, N., Dolbow, J. and Belytschko, T. (1999). A finite element method for crack growth without remeshing. Int. J. Num. Meths. in Engng., 46, 131-150.

[10] Sukumar, N., Möes, N., Moran, B. and Belytschko, T. (2000). Extended finite element method for three-dimensional crack modelling. Int. J. Num. Meths. in Engng., 48, 1549-1570.

[11] Simo, J.C., Oliver, J. and Armero, F. (1993). An analysis of strong discontinuities induced by strain-softening in rate-independent inelastic solids. Computational Mechanics, 12, 49-61.

[12] Oliver, J. (1995). Continuum modeling of strong discontinuities in solid mechanics using damage models. Computational Mechanics, 17, 277-296.

[13] Oliver, J., Cervera, M. and Manzoli, O. (1999). Strong discontinuities and continuum plasticity models: the strong discontinuity approach. Int. J. of Plasticity, 15, 319-351.

[14] Oliver, J., Huespe, A.E. Samaniego, E. and Chaves, W.V.. (2004). Continuum approach to the numerical simulation of material failure in concrete. Int. J. for Num. and Anal. Meth. in Geomechanics., 28, 609-632.

[15] Oliver, J. and Huespe, A.E. (2004). Theoretical and computational issues in modelling material failure in strong discontinuity scenarios. Comp. Meth. in Appl. Mech. and Eng., 193, 2987-3014.

[16] Oliver, J. and Huespe, A.E. (2004). Continuum approach to material failure in strong discontinuity settings. Comp. Meth. in Appl. Mech. and Eng., 193, 3195-3220.

[17] Feist, C., Kerber, W., Lehar, H. and Hofstetter, G. (2004). A comparative study of numerical models for concrete cracking. Proceedings of European Congress on Computational Methods in Applied Sciences and Engineering, ECCOMAS 2004, Neittaanmäki, P., Rossi, T., Korotov, S., Oñate, E., Periaux, J. and Knörzer, D. (eds.), Jyväskylä, Finland.

[18] Mosler, J. and Meschke, G. (2004). Embedded crack vs. smeared crack models: a comparison of elementwise discontinuous crack path approaches with emphasis on mesh bias. Comp. Meth. in Appl. Mech. and Eng., 193, 3351-3375.

[19] Rashid, Y. (1968). Analysis of prestrssed concrete pressure vessels. Nuclear Engineering and Design, 7, 334-344.

[20] Hillerborg, A., Modeer, M., and Peterson, P.E. (1976). Analysis of crack formation and crack growth in concrete by means of F. M. and finite elements. Cement and Concrete Research, 6, 773-782.

[21] Bazant, Z.P. and Oh, B.H. (1983). Crack band theory for fracture of concrete. Material and Structures, 16, 155-177.

[22] de Borst, R. (2002). Fracture in quasi-brittle materials: a review of continuum damage-based approaches. Engineering Fracture Mechanics, 69, 95-112.

[23] Cervera, M., Oliver, J., and Faria, R. (1995). Seismic evaluation of concrete dams via continuum damage models. Earth. Engng. Struc. Dyn., 24, 1225–1245.

[24] Cervera, M., Oliver, J., and Manzoli, O. (1996). A rate-dependent isotropic damage model for the seismic evaluation of concrete dams. Earth. Engng. Struc. Dyn., 25, 987–1010.

[25] Finchant, S, La Borderie, C. and Pijaudier-Cabot, G. (1999). Isotropic and anisotropic descriptions of damage in concrete structures. Mechanics of Cohesive-Frictional Materials, 4, 339-359.

[26] Aifantis, E.C., 1984. On the microstructural origin of certain inelastic models. Transactions ASME Journal of Engineering Materials Technology, 106, 326-330.

[27] de Borst, R. and Mulhaus, H.B. (1992). Gradient-dependent plasticity: formulation and algorithm aspect. Int. J. Num. Meths. in Engng., 35, 521-539.

[28] Peerlings, R.H.J., de Borst, R., Brekelmans, W.A. M. and Geers, M.G.D. (1998). Gradient-enhanced damage modelling of concrete failures. Mechanics of Cohesive-Frictional Materials, 4, 339-359.

[29] de Borst, R. (2001). Some recent issues in computational failure mechanics. Int. J. Num. Meths. in Eng., 52, 63-95.

[30] Bazant, Z. and Jirásek, M. (2002). Nonlocal Integral Formulations of Plasticity and Damage: Survey of Progress. J. of Engineering Mechanics, ASCE, 128, 1119-1149.

[31] Oliver, J. (1989). A consistent characteristic length for smeared cracking models. Int. J. Num. Meth. Engng., 28, 461–474.

[32] Dumstorff, P. and Meschke, G. (2004). Investigation of crack growth criteria in the context of the extended finite element method. Proceedings of European Congress on Computational Methods in Applied Sciences and Engineering, ECCOMAS 2004, Neittaanmäki, P., Rossi, T., Korotov, S., Oñate, E., Periaux, J. and Knörzer, D. (eds.), Jyväskylä, Finland.

[33] Grassl, P. and Jirásek, M. (2004). On mesh bias of local damage models for concrete: In *Fracture Mechanics of Concrete Structures,* Proceedings of 5th Int. Conference on Fracture Mechanics of Concrete and Concrete Structures, FraMCoS-5, V. C. Li et al. (eds.), Vail, Colorado, U.S.A.

[34] Cervera, M., Chiumenti and Agelet de Saracibar, C. (2002). COMET: COupled MEchanical and Thermal analysis. Data Input Manual, Version 5.0, Technical report IT-308, www.cimne.upc.es.

[35] GiD: the personal pre and post-processor (2002). www.gid.cimne.upc.es.

[36] Nooru-Mohamed, M.B. (1992), Mixed mode fracture of concrete: an experimental approach. Ph. D. Thesis, TU Delft, The Netherlands.

[37] Di Prisco, M., Ferrara, L., Meftah, F., Pamin, J., de Borst, R., Mazars, J. and Reynouard, J.M. (2000). Mixed mode fracture in plain and reinforced concrete: some results on benchmark tests. Int. J. of Fracture, 103, 127-148.

[38] Pazák, B. and Jirásek, M. (2003). Adaptive simulation of quasibrittle failure: In *Computational Modelling of Concrete Structures,* Proceedings of EURO-C 2003 Conference, Bicanic, N., de Borst, R., Mang, H. and Meschke, G. (eds.), St. Johann im Pongau, Austria. A.A. Balkema Publishers.